# Synthesis, X-ray Structural Determination, and Magnetic Susceptibility, Mössbauer, and EPR Studies of $(Ph_4P)_2[Fe_2(Cat)_4(H_2O)_2]\cdot 6H_2O$, a Catecholato-Bridged Dimer of Iron(III)

**Vincent A. Grillo,[1a] Graeme R. Hanson,*[,1b] Deming Wang,[1b] Trevor W. Hambley,[1c] Lawrence R. Gahan,[1a] Keith S. Murray,[1d] Boujemaa Moubaraki,[1d] and Clifford J. Hawkins[1a,e]**

Chemistry Department and Centre for Magnetic Resonance, The University of Queensland, Brisbane, QLD 4072 Australia, The School of Chemistry, The University of Sydney, Sydney, NSW 2006 Australia, and Chemistry Department, Monash University, Clayton, Victoria 3168, Australia

*Received April 26, 1995*[⊗]

Reaction of $Fe(OH)_3$ with 2 equiv of catechol (Cat) and 1 equiv of NaOH in aqueous solution produces violet crystals (monoclinic unit cell, space group *C*2/*c*, with $a = 22.544(9)$ Å, $b = 12.949(6)$ Å, $c = 22.459(9)$ Å, $\beta = 91.10(3)°$, $V = 6555(5)$ Å$^3$, $Z = 4$, and $R = 0.039$) of $(Ph_4P)_2[Fe_2(Cat)_4(H_2O)_2]\cdot 6H_2O$. X-ray crystallography reveals that the complex consists of an anionic binuclear iron(III) core in which each iron is coordinated by six oxygen atoms with the two $FeO_6$ octahedra sharing a common edge. The complex is centrosymmetric with an inversion center in the middle of the $Fe_2O_2$ core. The Fe···Fe distance is 3.272(1) Å, and the bridging Fe−O(1)−Fe angle is 106.2°. Bridging catechol ligands are coplanar, and the nonbridging catechol ligands and coordinated water molecules are located *trans* to the $Fe_2O_2$ plane. Infrared spectra of $(Ph_4P)_2[Fe_2(Cat)_4(H_2O)_2]\cdot 6H_2O$ show characteristic C−O stretching frequencies at 1475 and 1432 cm$^{-1}$, and the absorption spectrum in dimethyl sulfoxide is dominated by an intense broad peak at 18 350 cm$^{-1}$ ($\epsilon_{max} = 3430$ M$^{-1}$ cm$^{-1}$). Variable temperature magnetic susceptibility data show that the two iron(III) sites are weakly antiferromagnetically coupled ($J = -9.7$ cm$^{-1}$, $g = 2.00$, $p$(%monomer) = 5.2%). X- and Q-band EPR spectra are interpreted in terms of the strong exchange limit, and the resonances arise from an $S_T = 1$ spin multiplet ($g = 1.95 \pm 0.01$, $|D| = 0.052 \pm 0.003$ cm$^{-1}$, $|E| = 0.013 \pm 0.001$ cm$^{-1}$, and $E/D = 0.25$) and an $S_T = 2$ spin multiplet ($g = 1.93 \pm 0.02$, $|D| = 0.041 \pm 0.002$ cm$^{-1}$, $|E| = 0.0102 \pm 0.0005$ cm$^{-1}$, and $E/D = 0.25$). Mössbauer spectra of the complex at 4.2 K in zero applied magnetic field were fitted with a single quadrupole split doublet with an isomer shift of 0.556 mm s$^{-1}$ and a quadrupole splitting of 0.898 mm s$^{-1}$.

## Introduction

Iron(III) catecholate (Cat)[2] chemistry has been extensively studied because of its relevance to biological systems such as bacterial siderophores, biologically important catecholamines, the catechol binding dioxygenases, and DOPA containing proteins.[3−7] The suggestion has even been made that the role of the DOPA-protein ferreascidin from the ascidian *Pyura stolonifera*, which binds to iron(III) via two catechol residues, is in curing the DOPA protein for the repair of wounds and/or for securement of the ascidian to its substratum.[4,5]

The binding of catechol or catechol type ligands to iron(III) has been investigated extensively.[8−23] Monomeric complexes such as $[Fe(Cat)_3]^{3-}$,[8−11] models for enterobactin[11−13] and mixed ligand systems, such as $(Ph_4P)[Fe(bpy)(Cl_4(Cat))_2]$ [14] and $[Fe(acac)(Cat)_2]^{3-}$,[15] as well as binuclear iron(III) catechol complexes have been reported.[8,16,17] Anderson *et al.*[8,16] isolated a purple complex, characterized as $(pipH)_3[Fe_2(Cat)_4(OAc)]$,

⊗ Abstract published in *Advance ACS Abstracts,* May 1, 1996.

(1) (a) The Chemistry Department, The University of Queensland. (b) Centre for Magnetic Resonance, The University of Queensland. (c) The University of Sydney. (d) Monash University. (e) Present address: ICT Pharmaceuticals, P.O. Box 228, Brookvale, NSW, Australia, 2100.

(2) Abbreviations: acac, acetylacetonate; $bipH_2$, 1,1′-biphenyl-2,2′-diol; bpy, bipyridine; $CatH_2$, catechol; $DBCatH_2$, 3,5-di-*tert*-butylcatechol; DBSQ, 3,5-di-*tert*-butyl-1,2-semiquinonate; DMF, dimethylformamide; DMSO, dimethyl sulfoxide; DOPA, 3,4-dihydroxyphenylalanine; en, ethylenediamine; ent, enterobactin; Et, ethyl; MECAM, 1,3,5-tris(2,3-dihydroxybenzoyl)amino)methyl)benzene; $Me_3[9]aneN_3$, *N*,*N*′,*N*″-trimethyl-1,4,7-triazacyclononane; $ntaH_3$, nitrilotriacetic acid; OAc, acetate; ph, phenyl; pip, piperidine; py, pyridine; SQ, 1,2-semiquinonate.

(3) Matzanke, B. F.; Muller-Matzanke, G.; Raymond, K. N. In *Iron Carriers and Iron Proteins;* Loehr, T. M., Ed.; Physical Bioinorganic Series; VCH Publishers: New York, 1989, pp 1−121.
(4) Taylor, S. W.; Hawkins, C. J.; Winzor, D. J. *Inorg. Chem.* **1993**, *32*, 422.
(5) Taylor, S. W.; Cashion, J. D.; Brown, L. J.; Hawkins, C. J.; Hanson, G. R. *Inorg. Chem.* **1995**, *34*, 1487.
(6) Raymond, K. N.; Muller, G.; Matzanke, B. F. *Top. Curr. Chem.* **1984**, *123*, 49.
(7) Taylor, S. W.; Luther, G. W.; Waite, J. H. *Inorg. Chem.* **1994**, *33*, 5819.
(8) Anderson, B. F.; Buckingham, D. A.; Robertson, G. B.; Webb, J.; Murray, K. S.; Clark, P. E. *Nature* **1976**, *262*, 722.
(9) Raymond, K. N.; Isied, S. S.; Brown, L. D.; Fronczek, F. R.; Nibert, J. H. *J. Am. Chem. Soc.* **1976**, *98*, 1767.
(10) Karpishin, T. B.; Gebhard, M. S.; Solomon, E. I.; Raymond, K. N. *J. Am. Chem. Soc.* **1991**, *113*, 2977.
(11) Avdeef, A.; Sofen, S. R.; Bregante, T. L.; Raymond, K. N. *J. Am. Chem. Soc.* **1978**, *100*, 5362.
(12) Cox, D. D.; Que, L., Jr. *J. Am. Chem. Soc.* **1988**, *110*, 8085.
(13) Pecoraro, V. L.; Wong, G. B.; Kent, T. A.; Raymond, K. N. *J. Am. Chem. Soc.* **1983**, *105*, 4617.
(14) Zirong, D.; Bhattacharya, S.; McCusker, J. K.; Hagen, P. M.; Hendrickson, D. N.; Pierpont, C. G. *Inorg. Chem.* **1992**, *31*, 870.
(15) Buckingham, D. A.; Clark, C. R.; Weller, M. G.; Gainsford, G. J. *J. Chem. Soc., Chem. Comm.* **1982**, 779.
(16) Anderson, B. F.; Webb, J.; Buckingham, D. A.; Robertson, G. B. *J. Inorg. Biochem.* **1982**, *16*, 21.
(17) Zirong, D.; Haltiwanger, R. C.; Bhattacharya, S.; Pierpont, C. G. *Inorg. Chem.* **1991**, *30*, 4288.
(18) Hider, R. C.; Mohd-Nor, A. R.; Silver, J.; Morrison, I. E. G.; Rees, L. V. C. *J. Chem. Soc., Dalton Trans.* **1981**, 609.
(19) Linert, W.; Jameson, R. F.; Herlinger, E. *Inorg. Chim. Acta* **1991**, *187*, 239.
(20) Hider *et al.* describe the bis(catecholato) iron(III) complex as $[Fe(Cat.H)(Cat.)(OH)]^-$.[18]
(21) Mentasti, E.; Pelizzetti, E. *J. Chem. Soc., Dalton Trans.* **1973**, 2605.
(22) Mentasti, E.; Pelizzetti, E.; Saini, G. *J. Inorg. Nucl. Chem.* **1976**, *38*, 785.
(23) Mentasti, E.; Pelizzetti, E.; Saini, G. *J. Chem. Soc., Dalton Trans.* **1973**, 2609.

S0020-1669(95)00499-X CCC: $12.00 

where, in addition to the bridging catechol ligands, a bridging acetate ion was present. The isolation and characterization of $(Ph_4P)_2[Fe_2Cl_4(Cat)_2]$, where again one oxygen from each catechol moiety bridges the two iron(III) sites, has also been reported.[17]

There has been some conjecture as to the exact nature and oxidation state of the iron complexes formed with catecholato or catecholato type ligands, under various pH[18] and anaerobic versus aerobic conditions.[19] Titration of iron(III) chloride catechol solutions (1:1, 1:3, and 1:6) with base produces yellow, green, blue, purple, and wine-red colored solutions as the pH is increased from 1 to 12. The optical spectra of these latter four solutions exhibit intense catecholate to iron(III) charge transfer bands which are sensitive to the coordination environment of the metal ion and are therefore useful diagnostics of the species present in solution ($[Fe^{III}(Cat)(H_2O)_4]^+$, $\lambda_{max} = 700$ nm, $\epsilon = 1500$ $M^{-1}$ $cm^{-1}$; $[Fe^{III}(Cat)_2]^-$,[20] $\lambda_{max} = 570$ nm, $\epsilon = 3330$ $M^{-1}$ $cm^{-1}$; $[Fe^{III}(Cat)_3]^{3-}$, $\lambda_{max} = 490$ nm, $\epsilon = 4190$ $M^{-1}$ $cm^{-1}$).[11] In conjunction with potentiometric and conductivity titrations and Mössbauer spectra, a detailed description of the formation equilibria (eq 1) has been given by Hider.[18] Below

$$[Fe^{III}(H_2O)_6]^{3+} + CatH_2 \rightleftharpoons [Fe^{III}(Cat)(H_2O)_4]^+ + 2H_3O^+$$

$$[Fe^{III}(Cat)(H_2O)_4]^+ \rightleftharpoons [Fe^{II}(SQ)(H_2O)_4]^+$$

$$[Fe^{II}(SQ)(H_2O)_4]^+ + 2CatH_2 \rightleftharpoons [Fe^{II}(CatH)_2(SQH)] + H^+$$

$$[Fe^{II}(CatH)_2(SQH)] + OH^- \rightleftharpoons [Fe^{II}(CatH)(SQ)(OH)]^- + CatH_2$$

$$[Fe^{II}(CatH)(SQ)(OH)]^- \rightleftharpoons [Fe^{III}(CatH)(Cat)(OH)]^-$$

$$[Fe^{II}(CatH)_2(SQH)] + [Fe^{III}(CatH)(Cat)(OH)]^- \rightleftharpoons [Fe_2^{III}(Cat)_4(\mu\text{-}OH)]^{3-} + CatH_2 + 2H^+$$

$$[Fe_2^{III}(Cat)_4(\mu\text{-}OH)]^{3-} + 2CatH^- \rightleftharpoons 2[Fe^{III}(Cat)_3]^{3-} + H_3O^+ \quad (1)$$

pH 4.0 formation of the green complex $[Fe^{III}(Cat)(H_2O)_4]^+$ occurs.[11,18,19,21,22] Upon intramolecular electron transfer the semiquinone complex $[Fe^{II}(SQ)(H_2O)_4]^+$ forms which can subsequently decompose to catechol and iron(III).[18,21,23] Above pH 9.5 the wine-red colored $[Fe(Cat)_3]^{3-}$ complex forms.[11,18] The species giving rise to the blue and purple solutions, which are present over the range of pH 6.5−9, have been assigned to $[Fe^{III}(CatH)(Cat)(OH)]^-$ and $[Fe_2^{III}(Cat)_4(\mu\text{-}OH)]^{3-}$, respectively,[18] the latter assignment being based upon that of the purple complex $[Fe_2(Cat)_4(OAc)]^{3-}$.[16] However, there is some debate in the literature as to whether the purple species is in fact a unique species[18] or arises from a mixture of the bis- and tris-(catecholato)iron(III) complexes.[11]

As part of ongoing research in this area we report herein the preparation, isolation, and characterization, by X-ray crystallography, magnetic susceptibility measurements, infrared, ultraviolet−visible, EPR,[24] and Mössbauer spectroscopy of a binuclear iron(III) complex of stoichiometry $[Fe(C_6H_4O_2)_2(H_2O)]^-$ isolated as the tetraphenylphosphonium salt. The anion contains bidentate and bridging catecholato ligands and a bound water molecule. The present study provides an insight into the formation equilibria of iron catecholate species and demonstrates the capacity of a recently developed computer simulation software package, SOPHE,[25,26] to quantitatively characterize EPR spectra from exchange coupled binuclear iron complexes.

(24) The International EPR Society is recommending that the acronym EPR rather than ESR be used to describe this technique.

## Experimental Section

**Chemicals and Physical Methods.** Catechol was recrystallized from toluene. $FeCl_3 \cdot 6H_2O$ (A.R.) was purchased from UNILAB and used as supplied. Methanol was dried over magnesium methoxide and stored under dinitrogen. Distilled water was redistilled and stored under dinitrogen. Anaerobic manipulations were carried out under dry dinitrogen using standard Schlenk techniques with a double manifold vacuum line or in a VAC Vacuum/Atmospheres (HE-43-2) controlled atmospheres laboratory. Electronic absorption and infrared spectra were recorded with Beckman DU7500 and Mattson 400A Fourier transform infrared spectrophotometers, respectively. The infrared spectra were measured as KBr pellets.

**$(Ph_4P)_2[Fe_2(C_6H_4O_2)_4(H_2O)_2]\cdot 6H_2O$.** To a stirred solution of $FeCl_3 \cdot 6H_2O$ (5.00 g, 18.5 mmol) in $H_2O$ (15 mL), NaOH (2.59 g, 64.5 mmol) in $H_2O$ (15 mL) was added dropwise, resulting in precipitation of hydrous ferric oxide. The ferric oxide was isolated by centrifugation and repeatedly washed with $H_2O$ (3 × 20 mL). The "$Fe(OH)_3$" was transferred to a Schlenk tube, which was evacuated and purged with dinitrogen. To this was added degassed $H_2O$ (15 mL) followed by separate aqueous solutions (5.0 mL) of catechol (4.07 g, 37 mmol) and NaOH (0.74 g, 6.17 mmol), via a cannula. The resulting solution, pH 7.4, was stirred and heated at 60−70 °C for 0.5 h and then filtered through Celite while hot. The filtrate was permitted to cool to room temperature, and, on standing, the sodium salt precipitated (4.5 g, 80%). Metathesis with $Ph_4PCl$ in methanol produced dark purple crystals upon standing overnight at 4 °C. Anal. Calcd for $C_{72}H_{72}Fe_2O_{16}P_2$: C, 63.2; H, 5.31. Found: C, 62.7; H, 4.98.

**Magnetic Studies.** Magnetic susceptibility studies were made using a Quantum Design MPMS SQUID magnetometer with an applied field of 1 T. The powdered sample was contained in a calibrated gelatin capsule which was held in the center of a soda straw fixed to the end of the sample rod. The magnetization values of the instrument were calibrated against a standard palladium sample, supplied by Quantum Design, and also against chemical calibrants such as $CuSO_4 \cdot 5H_2O$ and $[Ni(en)_3](S_2O_3)$.

**Mössbauer Spectroscopy.** Mössbauer spectra were measured in the Physics Department at Monash University with a standard electromechanical transducer operating in a symmetrical constant acceleration mode. A conventional helium bath cryostat was employed for temperature control with the sample maintained in exchange gas. Data were collected with an LSI based 1000 channel multichannel analyzer. Velocity calibration was made with respect to iron foil. Spectra were fitted with a Lorentzian line shape.

**EPR Spectroscopy.** X- (9−10 GHz, $TE_{102}$ rectangular cavity) and Q-band (34 GHz, $TE_{011}$ cylindrical cavity) EPR spectra were measured on a Bruker ESP300E spectrometer. A flowthrough cryostat in conjunction with a Eurotherm (B-VT-2000) variable temperature controller provided temperatures of 120−140 K at the sample position in the cavity. Lower temperatures (minimum 1.8 K) were obtained with a flowthrough Oxford instruments ESR910 cryostat in conjunction with an Oxford instruments ITC-4 variable temperature controller. Spectrometer tuning, signal averaging, and subsequent data manipulation were performed with version 3.02 of Bruker's esp300e software. For all of the EPR spectra, the modulation frequency was 100 kHz and the modulation amplitude was always less than one-tenth of the linewidth at half-height. The microwave frequency and magnetic field were calibrated using an EIP 548B microwave frequency counter and a Bruker ER035M Gaussmeter, respectively.

Computer simulation of the EPR spectra was performed using version 1.0 of SOPHE[25,26] running on a SUN SPARCstation 10/30 workstation. SOPHE employs matrix diagonalization for the calculation of the eigenvalues/eigenvectors from which the resonant field positions and the transition probability[27] can be calculated. The field swept EPR

(25) Wang, D.; Hanson, G. R. *J. Magn. Res.* **1995**, *117*, 1.
(26) Wang, D.; Hanson, G. R. *Appl. Magn. Res.*, in press.
(27) Van Veen, G. *J. Magn. Res.* **1978**, *38*, 91.

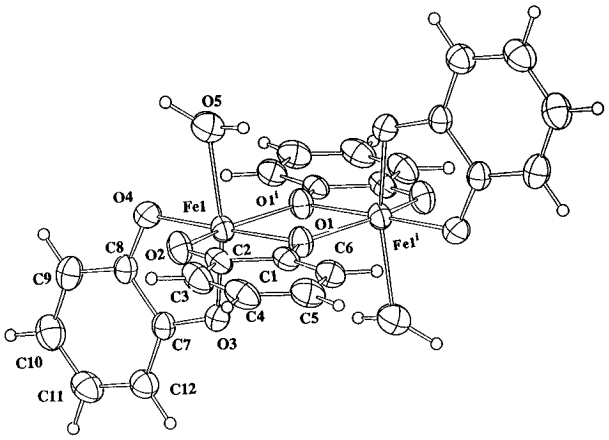


**Figure 1.** ORTEP plot of the complex anion $[Fe_2(Cat)_4(H_2O)_2]^{2-}$. $I = -x, -y, -z$.

**Table 1.** Selected Crystallographic Data for $(Ph_4P)_2[Fe_2(Cat)_4(H_2O)_2]\cdot 6H_2O$

| | | | |
|---|---|---|---|
| formula | $C_{72}H_{72}Fe_2O_{16}P_2$ | Z | 4 |
| fw | 1367.0 | $T$, K | 294 |
| space group | $C2/c$ | $\rho_{calcd}$, g cm$^{-3}$ | 1.385 |
| $a$, Å | 22.544(9) | $\lambda$ (Mo K$\alpha$), Å | 0.710 69 |
| $b$, Å | 12.949(6) | $\mu$ (Mo K$\alpha$), cm$^{-1}$ | 5.41 |
| $c$, Å | 22.459(9) | $R^a$ | 0.039 |
| $\beta$, deg | 91.10(3) | $R_w{}^b$ | 0.042 |
| $V$, Å$^3$ | 6555(5) | | |

$^a$ $R = \sum(||F_o| - |F_c||)/\sum|F_o|$. $^b$ $R_w = (\sum w(|F_o| - |F_c|)^2/\sum w|F_o|^2)^{1/2}$; $w = 1.8/(\sigma^2(F_o) + 0.00031F_o^2)$.

spectral intensity was normalized with the factor ($dB/d\nu$).[27] SOPHE also features a new method of partitioning the unit sphere in conjunction with global cubic spline and local linear interpolation. This allows randomly orientated powder spectra of high quality to be produced in significantly shorter times.

**X-ray Crystallography.** For diffractometry the crystal (violet prisms, 0.18 × 0.18 × 0.35 mm) was mounted on a glass fiber with cyanoacrylate resin. Lattice parameters at 21 °C were determined by least-squares fits to the setting parameters of 25 independent reflections, measured and refined on an Enraf-Nonius CAD4-F diffractometer with a graphite monochromator. Intensity data were collected in the range $1 < \theta < 25°$. Data were reduced and Lorentz, polarization, and numerical absorption corrections were applied using the Enraf-Nonius structure determination package (SDP). The structure was solved using the direct methods in SHELX-86[28] and was refined by full-matrix least-squares analysis with SHELX-76.[29] Neutral complex scattering factors were used.[30] Hydrogen atoms were included at calculated sites with fixed isotropic thermal parameters. All other atoms were refined anisotropically. Plots were drawn using ORTEP.[31] The atom numbering scheme is given in Figure 1. Selected crystallographic data are included in Table 1, final atomic coordinates are listed in Table 2, and listings of bond lengths and angles are given in Tables 3 and 4. The full crystallographic data, non-hydrogen atom thermal parameters, hydrogen atom coordinates and thermal parameters, and details of least-squares planes calculations are deposited as Supporting Information (Tables S1−S4).

## Results and Discussion

**Synthesis.** The synthesis of a binuclear iron(III) complex was achieved by the reaction of "$Fe(OH)_3$", 2 equiv of catechol, and 1 equiv of base in aqueous solution. Isolation of the sodium salt of bis(catecholato)iron(III) and subsequent metathesis with tetraphenylphosphonium chloride in methanol led to the binuclear iron(III) catechol complex $(Ph_4P)_2[Fe_2(Cat)_4(H_2O)_2]\cdot 6H_2O$ crystallizing as violet cubic crystals in high yield.

**Table 2.** Positional Parameters ($\times 10^4$) for $(Ph_4P)_2[Fe_2(Cat)_4(H_2O)_2]\cdot 6H_2O$

| | $x$ | $y$ | $z$ |
|---|---|---|---|
| Fe(1) | 241(1) | 919(1) | 442(1) |
| O(1) | −73(1) | 601(2) | −397(1) |
| O(2) | 139(1) | 2323(2) | 117(1) |
| C(1) | −164(1) | 1443(2) | −744(2) |
| C(2) | −51(1) | 2382(2) | −445(2) |
| C(3) | −133(1) | 3295(3) | −758(2) |
| C(4) | −304(1) | 3272(3) | −1350(2) |
| C(5) | −405(1) | 2356(3) | −1637(2) |
| C(6) | −345(1) | 1420(3) | −1330(2) |
| O(3) | 1100(1) | 771(2) | 309(1) |
| O(4) | 523(1) | 1240(2) | 1248(1) |
| C(7) | 1429(1) | 1084(2) | 780(1) |
| C(8) | 1113(1) | 1338(2) | 1294(1) |
| C(9) | 1417(2) | 1662(3) | 1801(2) |
| C(10) | 2022(2) | 1765(3) | 1796(2) |
| C(11) | 2329(2) | 1528(3) | 1300(2) |
| C(12) | 2036(1) | 1178(3) | 789(2) |
| O(5) | −599(1) | 1072(2) | 863(2) |
| P(1) | 2135(1) | 5364(1) | 1375(1) |
| C(13) | 2362(1) | 6688(2) | 1358(1) |
| C(14) | 1946(2) | 7469(3) | 1298(2) |
| C(15) | 2126(2) | 8490(3) | 1305(2) |
| C(16) | 2719(2) | 8718(3) | 1373(2) |
| C(17) | 3129(2) | 7955(3) | 1434(2) |
| C(18) | 2958(1) | 6935(3) | 1429(2) |
| C(19) | 1609(1) | 5218(2) | 1954(1) |
| C(20) | 1573(1) | 5936(3) | 2405(2) |
| C(21) | 1173(2) | 5796(3) | 2856(2) |
| C(22) | 811(1) | 4950(3) | 2859(2) |
| C(23) | 845(2) | 4245(3) | 2412(2) |
| C(24) | 1240(2) | 4377(3) | 1959(2) |
| C(25) | 2774(1) | 4593(2) | 1535(1) |
| C(26) | 3129(1) | 4269(3) | 1071(2) |
| C(27) | 3656(1) | 3778(3) | 1200(2) |
| C(28) | 3826(2) | 3592(3) | 1772(2) |
| C(29) | 3474(2) | 3902(3) | 2229(2) |
| C(30) | 2945(2) | 4398(3) | 2112(2) |
| C(31) | 1809(1) | 4954(3) | 682(1) |
| C(32) | 1590(2) | 5650(3) | 268(2) |
| C(33) | 1306(2) | 5286(5) | −245(2) |
| C(34) | 1258(2) | 4248(5) | −343(2) |
| C(35) | 1477(2) | 3559(4) | 55(2) |
| C(36) | 1754(2) | 3901(3) | 568(2) |
| O(6) | 1495(2) | −1079(3) | −70(2) |
| O(7) | 47(3) | 3859(4) | 936(3) |
| O(8) | −257(3) | 2292(7) | 1851(4) |
| O(9) | 0 | 476(28) | 2500 |

**Structure.** A view of the complex anion $[Fe_2(Cat)_4(H_2O)_2]^{2-}$ is presented in Figure 1. Complete listings of bond lengths and bond angles are given in Tables 3 and 4, respectively.

The complex consists of two $PPh_4^+$ cations and an anionic binuclear iron(III) core, where each iron is coordinated by six oxygen atoms with the two $FeO_6$ octahedra sharing a common edge. The complex ion is centrosymmetric with an inversion center in the middle of the $Fe_2O_2$ core. Each iron atom employs one oxygen donor, O(1), from the catecholate ligands to form the $Fe_2O_2$ unit, while the second oxygen atom, O(2), from this bridging catechol ligand is terminally coordinated to the iron(III) atom. In addition, each iron(III) ion is coordinated by a bidentate catecholato ligand, which does not participate in bridging the iron(III) core and a water molecule which makes up the sixth coordination site of the octahedron. The coordinated water molecules are located *trans* with respect to the $Fe_2O_2$ plane. The bridging catechol ligands are coplanar, with the

(28) Sheldrick, G. M. SHELXS-86. In *Crystallographic Computing 3;* Sheldrick, G. M., Krüger, C., Goddard, R., Eds.; Oxford University Press: Oxford, U.K., 1985; pp 175−189.
(29) Sheldrick, G. M. *SHELX-76, Program for Crystal Structure Determination*; University of Cambridge: Cambridge, U.K., 1976.
(30) Cromer, D. T.; Waber, J. T. *International Tables for X-ray Crystallography*; Kynoch Press: Birmingham, U.K., 1974; Vol. 4.
(31) Johnson, C. K. *ORTEP, A Thermal Ellipsoid Plotting Program;* Oak Ridge National Laboratory: Oak Ridge, TN, 1965.

**Table 3.** Bond Lengths (Å) for $(Ph_4P)_2[Fe_2(Cat)_4(H_2O)_2]\cdot 6H_2O$

| | | | |
|---|---|---|---|
| O(1)−Fe(1) | 2.046(2) | O(1)−Fe(1)[a] | 2.006(2) |
| O(2)−Fe(1) | 1.970(2) | O(3)−Fe(1) | 1.974(2) |
| O(4)−Fe(1) | 1.951(2) | O(5)−Fe(1) | 2.144(3) |
| C(1)−O(1) | 1.354(4) | C(2)−O(2) | 1.330(4) |
| C(2)−C(1) | 1.410(4) | C(6)−C(1) | 1.370(5) |
| C(3)−C(2) | 1.387(5) | C(4)−C(3) | 1.377(6) |
| C(5)−C(4) | 1.367(6) | C(6)−C(5) | 1.399(5) |
| C(7)−O(3) | 1.342(4) | C(8)−O(4) | 1.337(4) |
| C(8)−C(7) | 1.406(4) | C(12)−C(7) | 1.374(4) |
| C(9)−C(8) | 1.383(5) | C(10)−C(9) | 1.371(5) |
| C(11)−C(10) | 1.357(6) | C(12)−C(11) | 1.390(5) |
| C(13)−P(1) | 1.790(3) | C(19)−P(1) | 1.786(3) |
| C(25)−P(1) | 1.784(3) | C(31)−P(1) | 1.787(3) |
| C(14)−C(13) | 1.385(4) | C(18)−C(13) | 1.388(4) |
| C(15)−C(14) | 1.382(5) | C(16)−C(15) | 1.375(6) |
| C(17)−C(16) | 1.358(6) | C(18)−C(17) | 1.375(5) |
| C(20)−C(19) | 1.380(4) | C(24)−C(19) | 1.370(4) |
| C(21)−C(20) | 1.380(5) | C(22)−C(21) | 1.366(5) |
| C(23)−C(22) | 1.361(5) | C(24)−C(23) | 1.376(5) |
| C(26)−C(25) | 1.391(4) | C(30)−C(25) | 1.369(5) |
| C(27)−C(26) | 1.374(5) | C(28)−C(27) | 1.354(6) |
| C(29)−C(28) | 1.370(6) | C(30)−C(29) | 1.376(5) |
| C(32)−C(31) | 1.381(5) | C(36)−C(31) | 1.393(5) |
| C(33)−C(32) | 1.391(6) | C(34)−C(33) | 1.366(8) |
| C(35)−C(34) | 1.351(7) | C(36)−C(35) | 1.373(5) |

[a] $I = -x, -y, -z$.

**Table 4.** Bond Angles (deg) for $(Ph_4P)_2[Fe_2(Cat)_4(H_2O)_2]\cdot 6H_2O$

| | | | |
|---|---|---|---|
| Fe(1)−O(1)−Fe(2) | 106.2(1) | Fe(1)−O(1)−Fe(1)[a] | 107.7(1) |
| O(2)−Fe(1)−O(1) | 78.9(1) | O(3)−Fe(1)−O(1) | 99.5(1) |
| O(3)−Fe(1)−O(2) | 98.1(1) | O(4)−Fe(1)−O(1) | 178.6(1) |
| O(4)−Fe(1)−O(2) | 100.4(1) | O(4)−Fe(1)−O(3) | 81.8(1) |
| O(5)−Fe(1)−O(1) | 97.5(1) | O(5)−Fe(1)−O(2) | 88.9(1) |
| O(5)−Fe(1)−O(3) | 162.5(1) | O(5)−Fe(1)−O(4) | 81.2(1) |
| O(1)−Fe(1)−O(1)[a] | 72.2(1) | O(2)−Fe(1)−O(1)[a] | 150.1(1) |
| O(1)−Fe(1)−O(3)[a] | 94.7(1) | O(4)−Fe(1)−O(1)[a] | 108.2(1) |
| O(1)−Fe(1)−O(5)[a] | 86.9(1) | C(1)−O(1)−Fe(1) | 114.5(2) |
| C(2)−O(2)−Fe(1) | 116.0(2) | C(2)−C(1)−O(1) | 113.3(3) |
| C(6)−C(1)−O(1) | 125.0(3) | C(6)−C(1)−C(2) | 121.6(3) |
| C(1)−C(2)−O(2) | 117.1(3) | C(3)−C(2)−O(2) | 124.7(3) |
| C(3)−C(2)−C(1) | 118.2(3) | C(4)−C(3)−C(2) | 120.2(3) |
| C(5)−C(4)−C(3) | 121.0(4) | C(6)−C(5)−C(4) | 120.4(4) |
| C(5)−C(6)−C(1) | 118.6(3) | C(7)−O(3)−Fe(1) | 112.3(2) |
| C(8)−O(4)−Fe(1) | 113.4(2) | C(8)−C(7)−O(3) | 115.9(3) |
| C(12)−C(7)−O(3) | 124.9(3) | C(12)−C(7)−C(8) | 119.2(3) |
| C(7)−C(8)−O(4) | 115.6(3) | C(9)−C(8)−O(4) | 124.7(3) |
| C(9)−C(8)−C(7) | 119.7(3) | C(10)−C(9)−C(8) | 120.0(3) |
| C(11)−C(10)−C(9) | 120.6(4) | C(12)−C(11)−C(10) | 120.6(3) |
| C(11)−C(12)−C(7) | 119.9(3) | C(19)−P(1)−C(13) | 108.1(1) |
| C(25)−P(1)−C(13) | 108.0(1) | C(25)−P(1)−C(19) | 109.7(1) |
| C(31)−P(1)−C(13) | 112.3(1) | C(31)−P(1)−C(19) | 109.6(1) |
| C(31)−P(1)−C(25) | 109.0(1) | C(14)−C(13)−P(1) | 120.5(2) |
| C(18)−C(13)−P(1) | 119.7(2) | C(18)−C(13)−C(14) | 119.7(3) |
| C(15)−C(14)−C(13) | 119.9(3) | C(16)−C(15)−C(14) | 119.5(4) |
| C(17)−C(16)−C(15) | 120.9(4) | C(18)−C(17)−C(16) | 120.5(4) |
| C(17)−C(18)−C(13) | 119.5(3) | C(20)−C(19)−P(1) | 120.9(2) |
| C(24)−C(19)−P(1) | 120.1(2) | C(24)−C(19)−C(20) | 119.0(3) |
| C(21)−C(20)−C(19) | 120.0(3) | C(22)−C(21)−C(20) | 120.5(3) |
| C(23)−C(22)−C(21) | 119.5(3) | C(24)−C(23)−C(22) | 120.5(3) |
| C(23)−C(24)−C(19) | 120.5(3) | C(26)−C(25)−P(1) | 119.4(2) |
| C(30)−C(25)−P(1) | 120.4(2) | C(30)−C(25)−C(26) | 119.9(3) |
| C(27)−C(26)−C(25) | 119.3(3) | C(28)−C(27)−C(26) | 120.7(4) |
| C(29)−C(28)−C(27) | 120.1(3) | C(30)−C(29)−C(28) | 120.4(4) |
| C(29)−C(30)−C(25) | 119.6(3) | C(32)−C(31)−P(1) | 121.9(3) |
| C(36)−C(31)−P(1) | 119.0(2) | C(36)−C(31)−C(32) | 119.0(3) |
| C(33)−C(32)−C(31) | 119.4(4) | C(34)−C(33)−C(32) | 120.0(4) |
| C(35)−C(34)−C(33) | 121.1(4) | C(36)−C(35)−C(34) | 119.8(4) |
| C(35)−C(36)−C(31) | 120.6(3) | O(6)−H(6A)−O(3) | 174(6) |
| O(7)−H(7B)−O(2) | 165(7) | | |

[a] $I = -x, -y, -z$.

nonbridging catechol ligands located *trans* to the $Fe_2O_2$ plane. There are six water molecules in the lattice.

Similar binuclear iron(III) catecholate-bridged complexes with a planar $Fe_2O_2$ core have been reported. The complex $(pipH)_3[Fe_2(Cat)_4(OAc)]$[8,16] has two $FeO_6$ octahedra which share a common edge using oxygens of the two catechol dianions. In this case adjacent apical coordination sites are bridged by an acetate ion. As well, each octahedron contains one bidentate catechol moiety which is not involved in bridging the two iron(III) ion sites. The complex $(Ph_4P)_2[Fe_2Cl_4(Cat)_2]$ contains an $Fe_2O_2$ core in which the iron atoms exhibit distorted trigonal bipyramidal geometries.[17] While one of the oxygen donors of the catecholato ligand bridges the two iron(III) sites, the second oxygen atom from this bridging catechol ligand is coordinated to a single Fe(III) atom in an apical site. Chlorine atoms are located in the trigonal plane in which the bridging oxygen resides.[17] More structurally complex examples include the tetranuclear iron complexes $[Fe_4(DBSQ)_4(DBCat)_4]$,[32] $[Fe_4(DBCat)_4(py)_6]$,[33] and $(Et_4N)_3[MoFe_4S_4(SEt)_3(Cat)_3]$[34] in which the tris chelate $[Fe(Cat)_3]^{3-}$ subunit acts as a tridentate ligand to molybdenum.

In $[Fe_2(Cat)_4(H_2O)_2]^{2-}$ the Fe−O(1) bond distances (2.046(2) and 2.006(2) Å) for the bridging catecholate oxygen are longer than the Fe−O(2) distance (1.970 (2) Å) exhibited by the terminal oxygen from the same catecholate unit. The nonbridging catecholate exhibits two different Fe−O bond distances (Fe−O(4) 1.951(2) Å and Fe−O(3) 1.974(2) Å). The former bond length (Fe−O(4)), associated with the oxygen *trans* to the bridging catecholate oxygen and located in the $Fe_2O_2$ plane, is shorter than that below the plane (Fe−O(3)). For $(pipH)_3[Fe_2(Cat)_4(OAc)]$ the Fe−O distances show similar variation, ranging between 1.95(3) and 2.03(3) Å, and the Fe−O distance for the bridging oxygen donor (2.01(2) Å) is longer than that associated with the nonbridging oxygen donor (1.97(2) Å).[8,16] The increase in bond length upon bridging relative to terminal ligation has been observed previously in $[Fe_4(DBSQ)_4(DBCat)_4]$, which exhibits three coordination modes for the catecholate oxygen, *viz.*, terminal, $\mu_2$-bridging, and $\mu_3$-bridging with Fe−O bond lengths of 1.868(4), 2.000(4), and 2.183(4) Å, respectively.[32]

The Fe···Fe distance in $(Ph_4P)_2[Fe_2(Cat)_4(H_2O)_2]\cdot 6H_2O$ is 3.272(1) Å and is similar to that reported in other binuclear iron(III) catecholate-bridged complexes. For example, for $(Ph_4P)_2[Fe_2Cl_4(Cat)_2]$[17] and $(pipH)_3[Fe_2(Cat)_4(OAc)]$[8,16] the Fe···Fe distances are reported to be 3.299(1) and 3.217(7) Å, respectively.

The C−O bond distances in $[Fe_2(Cat)_4(H_2O)_2]^{2-}$ display a pattern similar to those in the analogous complex $[Fe_2Cl_4(Cat)_2]^{2-}$. In the two complexes the terminal C−O bond lengths (1.330(4) Å for $[Fe_2(Cat)_4(H_2O)_2]^{2-}$ and 1.328(7) Å for $[Fe_2Cl_4(Cat)_2]^{2-}$) are shorter than those observed for bridging groups (1.354(4) Å and 1.354(5) Å, respectively).[32] Ring C−C bond lengths are similar in both cases, with the (O−)C−C(−O) bond length longer than the other carbon−carbon bonds; e.g., C(1)−C(2) = 1.410(4) Å compared to $C-C_{av} = 1.380(6)$ Å for $[Fe_2(Cat)_4(H_2O)_2]^{2-}$. The question of charge distribution in metal quinone systems may be evaluated from the structural parameters.[35] The semiquinone ligands display shorter C−O bond lengths, and ring C−C bond lengths show the typical pattern displayed for complexes such as $[Fe(DBSQ)_3]$.[32] In the present case the Fe−O, C−O, and the C−C bond distances are all characteristic for catecholato ligation rather than semiquinone or quinone ligation.[32,33]

The $Fe-OH_2$ distance in $(Ph_4P)_2[Fe_2(Cat)_4(H_2O)_2]\cdot 6H_2O$ (2.144(3) Å) is typical of the bond distance displayed by other

(32) Boone, S. R.; Purser, G. H.; Chang, H.-R.; Lowery, M. D.; Hendrickson, D. N.; Pierpont, C. G. *J. Am. Chem. Soc.* **1989**, *111*, 2292.
(33) Shoner, S. C.; Power, P. P. *Inorg. Chem.* **1992**, *31*, 1001.
(34) Wolff, T. E.; Berg, J. M.; Holm, R. H. *Inorg. Chem.* **1981**, *20*, 174.
(35) Pierpont, C. G.; Buchanan, R. M. *Coord. Chem. Rev.* **1981**, *38*, 45.

iron(III) complexes, for example $[Fe(Me_3[9]aneN_3)(\mu\text{-}O)(\mu\text{-}OAc)_2Fe(bpy)(H_2O)](ClO_4)_2\cdot CH_2Cl_2$[36] and $Ba[\{Fe_2(nta)_2(H_2O)\}_2O]\cdot 4H_2O$[37] exhibit Fe−O($H_2O$) bond distances of 2.153(9) Å and $2.17_{av}$ Å, respectively.

**Electronic and Infrared Spectroscopy.** The infrared spectrum of $(Ph_4P)_2[Fe_2(Cat)_4(H_2O)_2]\cdot 6H_2O$ shows characteristic C−O stretching frequencies in the region of 1400−1500 $cm^{-1}$, with two bands at 1475 and 1432 $cm^{-1}$. The iron(III) catecholato complexes $[Fe(ent)]^{3-}$ and $[Fe(H_3ent)]^0$ (1460 and 1440 $cm^{-1}$) and $[Fe(MECAM)]^{3-}$ and $[Fe(H_3MECAM)]$ (1455 and 1435 $cm^{-1}$) display similar bands.[38] The band at 1260 $cm^{-1}$ has also been assigned to a C−O stretch on the basis of similar observations in metal−catecholate complexes.[39] Bands at 1568, 1318, and 1220 $cm^{-1}$ are tentatively assigned to the C=C stretching vibrational modes, while the peak at 1268 $cm^{-1}$ is assigned to the $\alpha_{CH}$ in plane deformation. Similar assignments have been made for catechol and other metal−catecholate systems.[38,40,41] Bands due to the benzene rings from the tetraphenylphosphonium ion, the counterion, may also overlap these bands. The broad peak at 3400 $cm^{-1}$ is due to the O−H stretch of the coordinated and solvated water molecules.

The electronic spectrum of the complex $(Ph_4P)_2[Fe_2(Cat)_4(H_2O)_2]\cdot 6H_2O$ in dimethyl sulfoxide is dominated by an intense broad peak at 18 350 $cm^{-1}$ ($\epsilon_{max}$ = 3430 $M^{-1}$ $cm^{-1}$). A small solvatochromic effect is observed for the complex with $\lambda_{max}$ = 18 050 $cm^{-1}$ ($\epsilon_{max}$ = 3430 $M^{-1}$ $cm^{-1}$) in dimethylformamide. $[Fe_2(Cat)_2Cl_4]^{2-}$ exhibits a broad absorption band at 17 120 $cm^{-1}$ ($\epsilon_{max}$ = 4500 $M^{-1}$ $cm^{-1}$) in dichloromethane,[17] whereas $(pipH)_3[Fe_2(Cat)_4(OAc)]$ exhibits a band at 17 540 $cm^{-1}$ ($\epsilon_{max}$ = 3400 $M^{-1}$ $cm^{-1}$) in water and in methanol at 17 860 $cm^{-1}$ ($\epsilon_{max}$ = 2700 $M^{-1}$ $cm^{-1}$).[16] The band observed in the spectra of these complexes has been ascribed to a ligand-to-metal charge transfer associated with the catecholato ligands.[10,11,17,42] The ligand-to-metal charge-transfer band characteristic for $[Fe(Cat)_3]^{3-}$ complexes has been found to be composed of two overlapping *x,y* polarized transitions at 18 414 and 22 018 $cm^{-1}$, both of which are ligand $\pi$ to metal d in character. It was proposed that a significant $\pi$ bonding contribution to the Fe−O interaction was present in these complexes.[10]

**Mössbauer Spectroscopy.** The Mössbauer spectrum of the complex $(Ph_4P)_2[Fe_2(Cat)_4(H_2O)_2]\cdot 6H_2O$ at 4.2 K in zero applied magnetic field and the nonlinear least squares fit is shown in Figure 2. The spectrum was fitted with a single quadrupole split doublet with an isomer shift of 0.556 mm $s^{-1}$ and a quadrupole splitting of 0.898 mm $s^{-1}$. The isomer shift is consistent with those observed for high-spin iron(III) ions in an octahedral or near-octahedral coordination.[43] The magnitude of the quadrupole splitting is a reflection of the unsymmetrical electric field gradient about each high-spin iron(III) site, although the two metal sites are equivalent. The complex $(pipH)_2[Fe_2(bipH)_4]$ with an analogous $Fe_2O_2$ core exhibits an isomer shift of 0.46 mm $s^{-1}$ and quadrupole splitting 0.65 mm $s^{-1}$, which indicate a more symmetric ligand field than that for $(Ph_4P)_2[Fe_2(Cat)_4(H_2O)_2]\cdot 6H_2O$.[44]

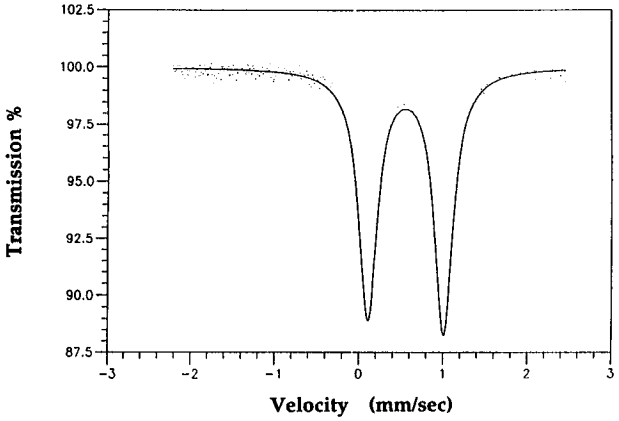


**Figure 2.** Mössbauer spectrum of $(Ph_4P)_2[Fe_2(Cat)_4(H_2O)_2]\cdot 6H_2O$ in zero applied magnetic field at 4.2 K.

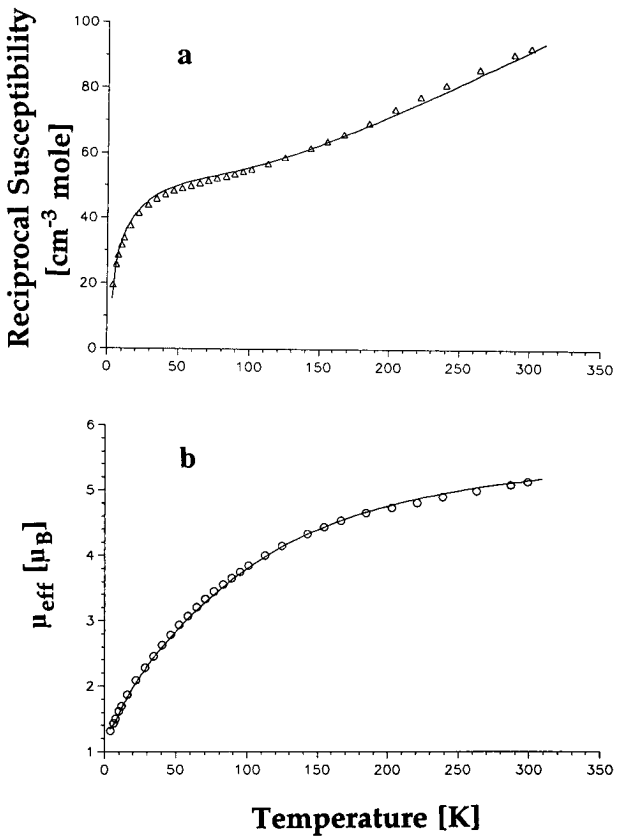


**Figure 3.** Plots of (a) the reciprocal magnetic susceptibility (per Fe) and (b) magnetic moment, $\mu_{eff}$ (per Fe), for $(Ph_4P)_2[Fe_2(Cat)_4(H_2O)_2]\cdot 6H_2O$ as a function of temperature. The solid lines are the calculated values using the parameter set $J$ = −9.7 $cm^{-1}$, $g$ = 2.00, and $p$(%monomer) = 5.2%.

**Magnetic Susceptibility.** The magnetic moment per Fe is 5.10 $\mu_B$ for $(Ph_4P)_2[Fe_2(Cat)_4(H_2O)_2]\cdot 6H_2O$, which is reduced from the $S = {}^5/_2$ value of 5.92 $\mu_B$ and is suggestive of antiferromagnetic coupling. Variable temperature solid-state magnetic susceptibility measurements were performed on a powdered sample of $(Ph_4P)_2[Fe_2(Cat)_4(H_2O)_2]\cdot 6H_2O$ over the temperature range 4.2−300 K. Plots of the reciprocal magnetic susceptibility and magnetic moment, per Fe, are displayed as a function of temperature in Figure 3. Normally for weakly coupled $d^5$−$d^5$ dimers a broad maximum in the susceptibility is anticipated with $\chi$ decreasing toward zero at very low temperatures. This does not occur here as a monomer "impu-

(36) Mauerer, B.; Crane, J.; Schuler, J.; Wieghardt, K.; Nuber, B. *Angew Chem., Int. Ed. Engl.* **1993**, *32*, 289.
(37) Heath, S. L.; Powell, A. K.; Utting, H.; Helliwell, M. *J. Chem. Soc., Dalton Trans.* **1992**, 305.
(38) Pecoraro, V. L.; Harris, W. R.; Wong, G. B.; Carrano, C. J.; Raymond, K. N. *J. Am. Chem. Soc.* **1983**, *105*, 4623.
(39) Wicklund, P. A.; Brown, D. G. *Inorg. Chem.* **1976**, *15*, 396.
(40) Hidalgro, A.; Otero, C. *Spectrochim. Acta* **1960**, *16*, 528.
(41) Wilson, H. W. *Spectrochim. Acta* **1974**, *30A*, 2141.
(42) Cox, D. D.; Benkovic, S. J.; Bloom, L. M.; Bradley, F. C.; Nelson, M. J.; Que, L., Jr.; Wallick, D. E. *J. Am. Chem. Soc.* **1988**, *110*, 2026.
(43) Greenwood, N. N.; Gibb, T. C. *Mössbauer Spectroscopy*; Chapman and Hall: London, 1971.
(44) Ainscough, E. W.; Brodie, A. M.; McLachlan, S. J.; Brown, K. L. *J. Chem. Soc., Dalton Trans.* **1983**, 1385.

rity" gives a superimposed Curie tail in susceptibility at low temperatures. The data were fitted with an expression derived from the Heisenberg−Dirac−van Vleck spin exchange Hamiltonian[45] $H = -2JS_1S_2$, where $S_1 = S_2 = {}^5/_2$. An additional Curie-law term in the susceptibility expression included *p*, the percentage of monomeric impurity. The best least squares fit (solid lines in Figure 3) gave the parameters $J = -9.7$ cm$^{-1}$, $g = 2.00$, and $p = 5.2\%$. The antiferromagnetic coupling of the two iron(III) ions is weak but does appear to be consistent with that reported for similar complexes, for example, $(pipH)_3[Fe_2(Cat)_4(OAc)]$[16] ($J = -10$ cm$^{-1}$) and $(pipH)_2[Fe_2(bipH)_4]$[44] ($J = -14$ cm$^{-1}$). For magnetically coupled bis($\mu$-alkoxo)diiron(III) complexes a quantitative relationship between the antiferromagnetic exchange interaction constant, *J*, and a structural parameter, *P*, which represents the length of the shortest superexchange pathway, has been proposed.[46]

$$-J = Ae^{BP} \tag{2}$$

where *A* ($8.763 \times 10^{11}$) and *B* ($-12.663$) are constants.[46] In this relationship the Fe−O−Fe angle is proposed to have only a second order effect, a conclusion reached previously.[47] *P* for $(Ph_4P)_2[Fe_2(Cat)_4(H_2O)_2]\cdot 6H_2O$ is 2.046 Å, resulting in a calculated value for *J* of $-5$ cm$^{-1}$. This result is similar to the experimentally determined value. Employing the same correlation for $(pipH)_3[Fe_2(Cat)_4(OAc)]$[16] ($P = 2.02$ Å) and $(pipH)_2[Fe_2(bipH)_4]$[44] (P = 2.011 Å) gave $J_{calc} = -7$ and $-8$ cm$^{-1}$, respectively.[46] The experimentally determined values were $-10$ and $-14$ cm$^{-1}$, respectively.[16,44] The results suggest that the primary contribution to the exchange in these dinuclear diiron(III) complexes is related to a parameter associated with the Fe−O bridge distance.[46]

**Electron Paramagnetic Resonance Spectroscopy.** The X- and Q-band solid-state EPR spectra of $(Ph_4P)_2[Fe_2(Cat)_4(H_2O)_2]\cdot 6H_2O$ (Figure 4) are well-resolved and can be characterized in terms of the strong exchange regime where the isotropic exchange coupling constant $J = -9.7$ cm$^{-1}$ dominates all of the other interactions. The spin system is then best characterized by the total spin operator $S_T = S_1 + S_2$. For two antiferromagnetically coupled $S = {}^5/_2$ ions, there are six possible spin multiplets characterized by $S_T = 0$, 1, 2, 3, 4, and 5, with $S_T = 0$ being the ground state. Each of these spin multiplets is $(2S_T + 1)$-fold degenerate. The energies for these spin multiplets are[48]

$$E(S_T) = -J[S_T(S_T + 1) - S_1(S_1 + 1) - S_2(S_2 + 1)] \tag{3}$$

and the energy difference between adjacent levels is

$$E(S_T) - E(S_T - 1) = -2S_TJ \tag{4}$$

The relative population ($I(S_T)$) of a given spin multiplet ($S_T$) for a pair of $S = {}^5/_2$ antiferromagnetically coupled ions has been given by Owen.[49]

$$I(S_T) = \frac{Ce^{JS_T(S_T+1)/kT}}{\sum_{S_T=0}^{5}(2S_T + 1)e^{JS_T(S_T+1)/kT}} \tag{5}$$

where *C* is a constant, *k* is the Boltzmann factor, and *T* is the temperature. The intensity of the resonances within the spin multiplet ($S_T$) is proportional to the transition probability[27] multiplied by $I(S_T)$ and the difference in Boltzmann populations ($e^{-E_i/kT} - e^{-E_j/kT}$) of the two resonant states ($|i\rangle$ and $|j\rangle$).

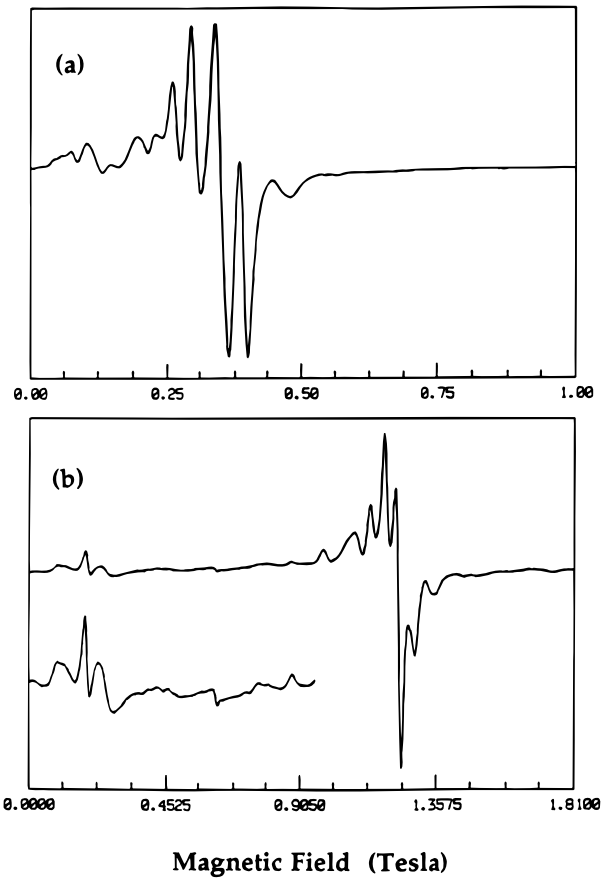


**Figure 4.** Multifrequency solid-state EPR spectra of $(Ph_4P)_2[Fe_2(Cat)_4(H_2O)_2]\cdot 6H_2O$: (a) $\nu = 9.4745$ GHz, $T = 125$ K; (b) $\nu = 33.9395$ GHz, $T = 130$ K.

A variable temperature (2−125 K) study of the X-band EPR spectrum of $(Ph_4P)_2[Fe_2(Cat)_4(H_2O)_2]\cdot 6H_2O$ is shown in Figure 5. For temperatures below about 10 K (Figure 5a,b), all of the excited-state multiplets are thermally depopulated and no EPR signal is expected from the $S_T = 0$ ground state. The resonances at $g = 8.77$, 4.25, and 0.57 (labeled with an asterisk in Figure 5a) are characteristic of a mononuclear high-spin iron(III) ion with an extreme rhombic distortion ($E/D = 1/3$) and can be interpreted in terms of the spin Hamiltonian

$$H = g\beta\mathbf{B}\cdot\mathbf{S} + D(S_z^2 - {}^1/_3S(S + 1)) + E(S_x^2 - S_y^2) \tag{6}$$

where $\beta$ is the Bohr magneton, **B** is the magnetic field, **S** is the electron spin operator, and *D* and *E* are the axial and rhombic fine structure parameters, respectively. The intensity of the $g = 8.77$, 4.25, and 0.57 resonances decreases as the temperature is raised. The presence of a mononuclear iron(III) complex, most likely $[Fe(Cat)(CatH)(OH)]^-$ or $[Fe(Cat)_2]^-$, is consistent with the *p* value from the magnetic susceptibility data. Since the ratio *E*/*D* indicates an orthorhombic symmetry, the catecholate ligands must be arranged in a *cis* arrangement with the fifth and sixth coordination sites filled with either aqua or hydroxy ligands. The weak signal around $g = 2.0$ is due to the cavity.

As the temperature was increased to approximately 12 K (Figure 5b and the inset), the resonances arising from the $S_T = 1$ multiplet begin to emerge. The two resonances symmetrically displayed about the $g = 2.0$ resonance with a separation of about 100 mT are indicative of $\Delta M_S = \pm 1$ transitions ($|1\rangle \leftrightarrow |0\rangle$ and $|-1\rangle \leftrightarrow |0\rangle$) within the $S_T = 1$ spin states. The linewidths are

(45) O'Connor, C. J. *Prog. Inorg. Chem.* **1982**, *29*, 203.
(46) Gorun, S. M.; Lippard, S. J. *Inorg. Chem.* **1991**, *30*, 1625.
(47) Thich, J. A.; Toby, B. H.; Powers, D. A.; Potenza, J. A.; Schugar, H. J. *Inorg. Chem.* **1981**, *20*, 3314.
(48) Bencini, A.; Gatteschi, D. *Electron Paramagnetic Resonance of Exchange Coupled Systems*; Springer-Verlag: Berlin, 1990.
(49) Owen, J. J. *Appl. Phys.* **1961**, *32*, 213S.

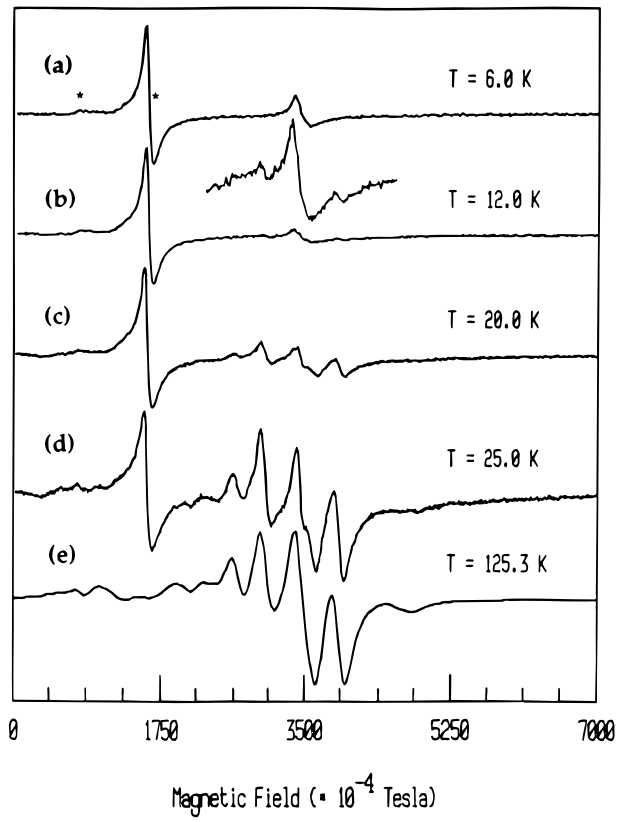


**Figure 5.** Variable temperature X-band EPR spectra for $(Ph_4P)_2[Fe_2(Cat)_4(H_2O)_2]\cdot 6H_2O$, (a) $\nu = 9.4491$ GHz, $T = 6$ K; (b) $\nu = 9.4487$ GHz, $T = 12$ K; (c) $\nu = 9.4437$ GHz, $T = 20$ K; (d) $\nu = 9.4487$ GHz, $T = 25$ K; (e) $\nu = 9.4745$ GHz, $T = 125$ K.

rather broad, typically 15−20 mT (full width at half-height). The intensity of the $S_T = 1$ resonances increased as the temperature was raised, reaching a relative maximum when $kT = -2J$. For $J = -9.7$ cm$^{-1}$, the temperature should be 28 K. Before the $S_T = 1$ resonances reach their maximum intensity, the $S_T = 2$ multiplet will have gained sufficient population to become EPR detectable. This is readily seen in Figure 5d, where the broad resonance at 480 mT emerges. The emergence of the $S_T = 2$ resonances and then the $S_T = 3$ resonances and so forth as the temperature is increased complicates the spectrum, especially in the $g = 2.0$ region. Therefore, we have only attempted to characterize the dominant EPR signals from the $S_T = 1$ and $S_T = 2$ multiplets using the spin Hamiltonian (fine structure and electron Zeeman interactions) in eq 6, where $S$ is replaced by $S_T$ and the electron Zeeman interaction is assumed to be isotropic.

Since the cavity background signal ($g = 2.0$) masks the $S_T = 1$ resonances at low temperatures, we used Figure 5d as the experimental spectrum where the $S_T = 1$ resonances reach their relative maximum intensity. A computer simulation (SOPHE, see Experimental Section) of the $S_T = 1$ resonances in this spectrum yielded $g = 1.95 \pm 0.01$, $|D| = 0.052 \pm 0.003$ cm$^{-1}$, $|E| = 0.013 \pm 0.001$ cm$^{-1}$, and $E/D = 0.25$. The large uncertainties are mainly due to the large linewidths. The values for the zero field splitting are small so that the temperatures (even at 2 K) were not low enough to allow the sign of $D$ be determined.

For the $S_T = 2$ multiplet, we believe the broad resonance centered at 480 mT (Figure 5e) defines the upper spectral boundary. In other words, this resonance arises from either the $|2\rangle \leftrightarrow |1\rangle$ ($D < 0$) or the $|-2\rangle \leftrightarrow |-1\rangle$ ($D > 0$) transition. In order to account for its linewidth which is about three times larger than the other main resonances in the spectrum (Figure 5e), we propose that this resonance is more likely due to two or more overlapping resonances. If this is true, the ratio $E/D$ must be close to 1/3. Under this assumption, the following values for the spin Hamiltonian parameters were obtained: $g = 1.93 \pm 0.02$, $|D| = 0.041 \pm 0.002$ cm$^{-1}$, $|E| = 0.0102 \pm 0.0005$ cm$^{-1}$, and $E/D = 0.25$. Again, the zero field splittings are rather small in comparison with the microwave quantum so that the X- and Q-band spectra (Figure 4a,b) are symmetrically displayed about $g = 2.0$. Although all of the resonances in the simulated spectrum could be located in the experimental spectrum (Figure 5e), there is one resonance at 260 mT in the experimental spectrum which could not be accounted for, and this resonance probably arises from the $S_T = 2$ multiplet. If this resonance is included, the ratio $E/D$ had to be reduced nearly to zero (axial symmetry) and the linewidth for the resonance at 480 mT in the simulated spectrum was less than half of the measured linewidth. We believe, therefore, that the interpretation with an $E/D$ ratio of 0.25 is the correct one for the $S_T = 2$ multiplet. The origin of the resonance at 260 mT is presently unknown.

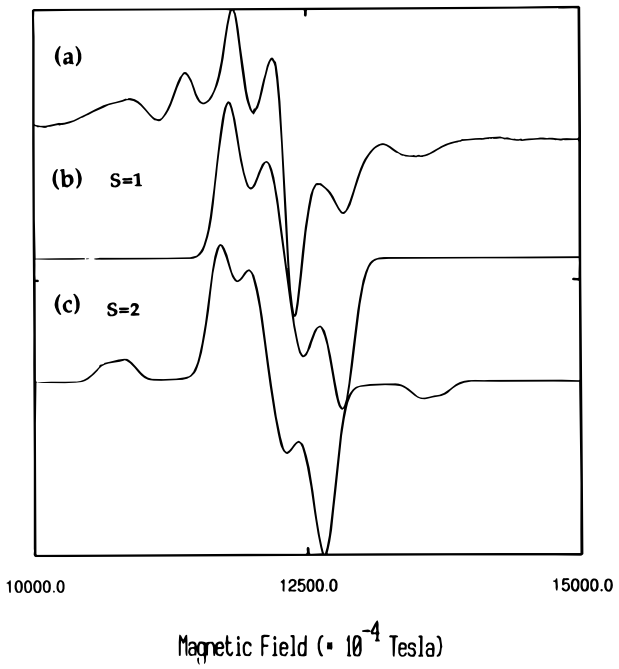


**Figure 6.** Experimental and computer simulated (SOPHE) spectra of the resonances in the $g = 2$ region: (a) experimental, $\nu = 33.9395$ GHz; (b) computer simulation of resonances arising from the $S_T = 1$ multiplet; (c) computer simulation of resonances arising from the $S_T = 2$ multiplet. Parameters for the simulations were as follows: partition number, $N = 19$ (190 vertex points); field axis resolution, 4096 points.

A comparison of parts b and a of Figure 4 demonstrates that the EPR spectrum is more dispersed at higher microwave frequencies, for example, at the Q-band. The above interpretation is consistent with a preliminary investigation of the Q-band (34.0 GHz) spectrum at 120 K. Using the values obtained through the simulation of the X-band spectra, the simulated Q-band spectra are shown in Figure 6b ($S_T = 1$)and Figure 6c ($S_T = 2$) and they agree well with the experimental spectrum (Figure 6a). Here again, the resonance at ∼1130 mT in the experimental spectrum which corresponds to the one at 260 mT at the X-band cannot be accounted for. Since the EPR spectra have been interpreted as arising from isolated spin multiplets, the intensites of the simulated spectra shown in parts b and c of Figure 6 have not been corrected for the relative population of the spin multiplets at 120 K. In addition to the intense resonances at $g \approx 2$ in the Q-band spectrum there are a few

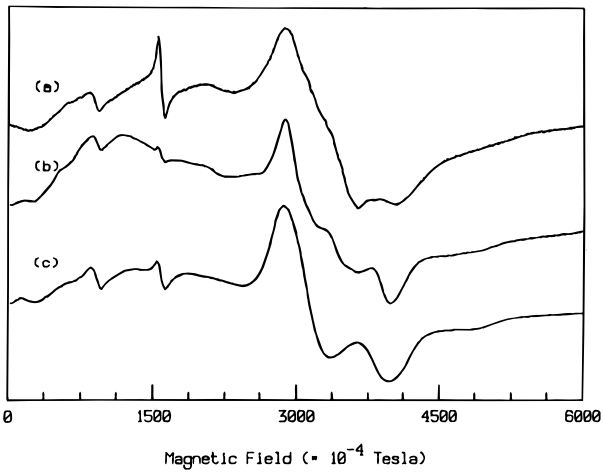


**Figure 7.** X-band EPR spectra of $(Ph_4P)_2[Fe_2(Cat)_4(H_2O)_2]\cdot 6H_2O$ dissolved in the following: (a) water, $\nu = 9.4701$ GHz; (b) DMF, $\nu = 9.4701$ GHz, $T = 125$ K; (c) DMSO, $\nu = 9.4701$ GHz, $T = 125$ K.

broad resonances below 200 mT, and these are not associated with either the $S_T = 1$ or $S_T = 2$ multiplets. They most likely arise from the $S_T = 3$ or higher spin multiplets. With higher gains, weak broad resonances are also observed at fields up to 1.83 T. A more detailed temperature dependent Q-band study of $(Ph_4P)_2[Fe_2(Cat)_4(H_2O)_2]\cdot 6H_2O$ is in progress in order to characterize the resonances belonging to the $S_T = 3$ and higher spin multiplets.

Dissolution of $(Ph_4P)_2[Fe_2(Cat)_4(H_2O)_2]\cdot 6H_2O$ in water, DMF, or DMSO results in marked changes to the X-band EPR spectrum (Figure 7), indicative of changes in the isotropic exchange coupling constant and the zero field splitting parameters. The similarity of the spectra recorded in protic and aprotic solvents suggests that the binuclear complex is maintained in solution, though in water dissociation occurs to a greater extent, producing the mononuclear $[Fe(Cat)_2]^-$ complex.

The isolation and X-ray crystallographic characterization of the purple $(Ph_4P)_2[Fe_2(Cat)_4(H_2O)_2]\cdot 6H_2O$ complex clearly shows that the equilibria (eq 1) describing the formation of the mono-, bis-, and hence tris(catecholato)iron(III) complexes are more complicated in that the $\mu$-hydroxy-bridged dimeric iron(III) complex[18] may be in equilibrium with the $[Fe_2(Cat)_4(H_2O)_2]^{2-}$ anion.

$$[Fe^{III}_2(Cat)_4(H_2O)_2]^{2-} + OH^- \rightleftharpoons [Fe^{III}_2(Cat)_4(\mu\text{-}OH)]^{3-} + 2H_2O \quad (7)$$

In conjunction with the equilibrium given in eq 1 this equilibrium may well explain the spectral differences observed in the solid state (Figure 4a) and the aqueous frozen solution (Figure 7a) EPR spectra. The differences between the frozen solution (Figure 7b, DMF; Figure 7c, DMSO) and solid state (Figure 4a) X-band EPR spectra of $(Ph_4P)_2[Fe_2(Cat)_4(H_2O)_2]\cdot 6H_2O$ and the observed solvatochromic shift of the wavelength maxima in the optical spectra presumably arise from the displacement of the aqua ligands or the bridging hydroxide by the organic solvent.

Interpretation of EPR spectra arising from exchange coupled spin systems has received considerable attention over the past decade as a consequence of the importance in characterizing the active sites in metalloproteins, for example, the $[3Fe-4S]^{1+,0}$ cluster containing metalloproteins[50,51] and the binuclear iron centers in non-heme iron proteins.[51−55] Exchange coupled binuclear transition metal ion centers can be classified into three regimes (weak, intermediate, and strong), according to the magnitude of the exchange coupling constant, $J$, with respect to the remaining spin Hamiltonian parameters for the complex.[48] Analytical solutions for the resonant field positions have been developed for systems in the strong and weak exchange regimes and have been widely used in the characterization of binuclear ($S_1 = S_2 = {}^1/_2$) copper and oxovanadium(IV) complexes[48,56] and coupled transition metal ion−radical species.[48,57] In certain circumstances spin systems in the intermediate regime can also be interpreted.[48]

For high-spin binuclear iron centers the weak, intermediate, and strong exchange regimes correspond to $|J| \ll |D|$, $|J| \sim |D|$, and $|J| \gg |D|$, respectively. The complexity of EPR spectra from spin systems within these regimes has been found to vary dramatically from one regime to another and even within a single regime. For example, the binuclear iron(II) centers in methane monooxygenase[53] and the azide complexes of deoxyhemerythrin[54] and the R2 protein of ribonucleotide reductase[55] exhibit weak asymmetric resonances around $g \sim 16$, arising from integer spin states of spin systems in the weak regime, while, for binuclear iron(III) centers in the strong and intermediate exchange regimes, EPR spectra may consist of either weak asymmetric resonances ($g \sim 12-18$), arising from integer spin states,[51,58] or resonances ranging from 0 to 1.8 T.[59]

Hendrich and DeBrunner[60] have developed a theory for interpreting EPR spectra from an $S = 2$ spin state of a magnetically isolated ion, and this has subsequently been applied successfully to EPR spectra from reduced [3Fe−4S] ferredoxins[51] and other binuclear iron complexes.[59] However, this theory has been found to be inadequate for the interpretation of the resonances around $g \sim 16$ found in the EPR spectra of non-heme iron proteins, and consequently the problem has been treated with either perturbation theory[59] or diagonalization of the complete energy matrix in the entire spin space.[53,55,58] These results clearly demonstrate that computer simulation of both the parallel ($B_1 | B_o$) and perpendicular ($B_1 \perp B_o$) mode EPR spectra is required for the quantitative determination of the spin Hamiltonian parameters.[51,53−55,58,60]

In contrast, characterization of randomly oriented EPR spectra from weakly antiferromagnetically coupled iron(III) and manganese(II) centers in the strong and intermediate exchange regimes has for the most part been qualitative.[59] For example, the complex EPR spectra arising from oxo- and hydroxo-bridged binuclear iron(III) complexes[44,59] have been assumed to arise from thermally populated coupled spin states of antiferromag-

(50) Kent, T. A.; Huynh, B. H.; Münck, E. *Proc. Natl. Acad. Sci.* **1980**, *77*, 6574.
(51) Münck, E.; Papaefthymiou, V.; Surerus, K. K.; Girerd, J.-J. In *Metal Clusters in Proteins*; ACS Symposium Series 372; Que, L., Jr., Ed.; American Chemical Society: Washington, D.C., 1988; p 302.
(52) Que, L., Jr.; Scarrow, R. C. In *Metal Clusters in Proteins*; Que, L., Jr., Ed.; ACS Symposium Series 372; American Chemical Society: Washington, D.C., 1988; p 152.
(53) Hendrich, M. P.; Münck, E.; Fox, B. G.; Lipscomb, J. D. *J. Am. Chem. Soc.* **1990**, *112*, 5861.
(54) Hendrich, M. P.; Pearce, L. L.; Que, L., Jr.; Chasteen, N. D.; Day, E. P. *J. Am. Chem. Soc.* **1991**, *113*, 3039.
(55) Elgren, T. E.; Hendrich, M. P.; Que, L., Jr. *J. Am. Chem. Soc.* **1993**, *115*, 9291.
(56) Smith, T. D.; Pilbrow, J. R. *Coord. Chem. Rev.* **1974**, *13*, 173.
(57) (a) Eaton, S. S.; Eaton, G. R. *Coord. Chem. Rev.* **1978**, *26*, 207. (b) Eaton, S. S.; Eaton, G. R. *Coord. Chem. Rev.* **1988**, *88*, 23.
(58) Fox, B. G.; Hendrich, M. P.; Surerus, K. K.; Andersson, K. K.; Froland, W. A.; Lipscomb, J. D.; Münck, E. *J. Am. Chem. Soc.* **1993**, *115*, 3688.
(59) Kurtz, D. M., Jr. *Chem. Rev.* **1990**, *90*, 585, and refererences cited therein.
(60) (a) Hendrich, M. P.; DeBrunner, P. G. *Biophys. J.* **1989**, *56*, 489. (b) Münck, E.; Surerus, K. K.; Hendrich, M. P. *Methods Enzymol.* **1993**, *227*, 463.

netically coupled ions, while Dismukes[61] has employed second order perturbation theory to predict the resonant field positions for several ferromagnetically coupled binuclear manganese(II) complexes as models for the binuclear manganese(II) center in manganese pseudocatalase.

Variable temperature X-band EPR spectra of the weakly antiferromagnetically coupled binuclear $(Ph_4P)_2[Fe_2(Cat)_4(H_2O)_2]\cdot 6H_2O$ complex revealed resonances from thermally populated $S_T = 1$ and $S_T = 2$ coupled spin states that are characteristic of spin systems in the strong exchange regime. Consequently, we have employed the computer simulation software SOPHE[25,26] to quantitatively determine the spin Hamiltonian parameters from the EPR spectra arising from the individual $S_T = 1$ and $S_T = 2$ coupled spin states. However, in addition to the intense resonances arising from the $S_T = 1$ and $S_T = 2$ coupled spin states, there are a large number of weaker resonances (Figure 4) that presumably arise from higher spin multiplets ($S_T = 3$, 4, and possibly 5). In conjunction with low-temperature (4−120 K) Q-band EPR measurements, where greater spectral resolution can be expected, the entire spectrum will be simulated as a function of temperature (Boltzmann factor included) with SOPHE using the following spin Hamiltonian

$$H = -2JS_1S_2 + S_1\cdot J_{aniso}\cdot S_2 + \sum_{i=1}^{2} S_i\cdot D_i\cdot S_i + \beta B\cdot g_i\cdot S_i \quad (8)$$

where $S_1 = S_2 = {}^5/_2$ and $S_1\cdot J_{aniso}\cdot S_2$ is the anisotropic exchange interaction. This new approach will potentially provide a detailed understanding of the spin-state origin of all of the resonances and yield the zero field splitting parameters for the individual iron(III) ions. SOPHE can be used to simulate EPR spectra from both magnetically isolated ($S \geq {}^1/_2$) and exchange-coupled ($S_1$, $S_2 \geq {}^1/_2$ for all three regimes) spin systems for the quantitative determination of the various spin Hamiltonian parameters.

**Acknowledgment.** This work was supported by Grants A29331095 and NSRG-21 awarded by the Australian Research Council and The University of Queensland, respectively. We thank Mr. Yassir Korbatieh and Prof. John D. Cashion for the measurement and analysis of the Mössbauer spectrum.

**Supporting Information Available:** Complete crystal data (Table S1), non-hydrogen atom thermal parameters ($\times 10^3$) (Table S2), hydrogen atom positional ($\times 10^4$) and thermal ($\times 10^3$) parameters (Table S3), and details of least-squares planes calculations for $(Ph_4P)_2[Fe_2(Cat)_4(H_2O)_2]\cdot 6H_2O$ (Table S4) (9 pages). Ordering information is given on any current masthead page.

IC950499B

(61) Mathur, P.; Crowder, M.; Dismukes, G. C. *J. Am. Chem. Soc.* **1987**, *109*, 5227.